

Atomistic investigation of dislocation-assisted carbon migration in iron

Tigany Zarrouk

October 28, 2020

Contents

1	Introduction	3
2	Computational Method	5
2.1	Peierls Potential	5
2.2	Preliminary calculations	7
2.3	Fe-C binding energies	8
2.4	Analysis of carbon concentration along dislocation	8
2.5	Line Tension Model	9
3	Results	10
3.1	Peierls Potential	10
3.2	Preliminary calculations	14
3.3	Fe-C binding energies	15
3.4	Analysis of carbon concentration along dislocation	19
3.5	Progression to Line Tension Model	21
4	Discussion	28
5	Future work	29
6	Conclusion	29
7	Appendix	30
7.1	Regularisation of interaction energy in quadrupolar array . . .	30
7.2	Zero-point energy calculation	31
8	Bibliography	31

Abstract

Martensitic bearing steels have been shown to undergo subsurface microstructural decay, forming Dark Etching Regions (DERs), promoting failure through rolling contact fatigue (RCF). Dislocation-assisted carbon migration is thought to be the underlying mechanism, yet empirical studies have been inconclusive as to how dislocations move carbon and where excess carbon from the martensitic matrix migrates to upon transformation to ferrite—a phase of significantly lower carbon solubility. In this report, we detail the first stage of a multi-scale modelling approach to elucidate carbon transport by dislocations. Tight-binding simulations of carbon interactions with the $1/2\langle 111 \rangle$ screw dislocation found solute distribution to vary significantly within $\sim 2b$ of the easy and hard cores; the highest binding energy being found in the centre of the hard screw core—which is the ground state carbon-dislocation configuration—in agreement with Density Functional Theory (DFT). Determination of equilibrium carbon concentration along dislocation lines, at various dislocation densities and nominal carbon concentrations, found most sites around the hard core were saturated, with all easy cores reconstructing to hard due to saturation of adjacent octahedral sites. In the typical temperature range of bearing operation, we expect all dislocations to be of hard core type, pinned by carbon in a prismatic site within the dislocation core. We anticipate large drag forces acting on dislocations in the initial stages of glide, due to carbon-dislocation binding. These atomistic results provide data for the last two stages in this multi-scale approach: determination of kink-pair formation energies as a function of stress and carbon concentration using a line tension model of a dislocation, and kinetic Monte Carlo (kMC) simulations incorporating solute diffusion, to ascertain how carbon moves with dislocations in different stress, temperature and concentration regimes.

1 Introduction

Martensitic steels are frequently used in bearings due to their resilience to service conditions, being subject to high rotational speeds and contact pressures. However, under cyclic loading exceeding a given contact stress, the microstructure of the steel can decay due to the accumulation of plasticity. This signals the onset of rolling cycle fatigue (RCF), which increases the risk of failure from subsurface crack initiation. The microstructural decay corresponds to the observation of Dark Etching Regions (DERs) as seen in optical microscopy, where the darkness of these regions is due to the higher reactivity of DER phases to the etchant; exacerbated by the roughness of the DER region [1]. See figure 1.

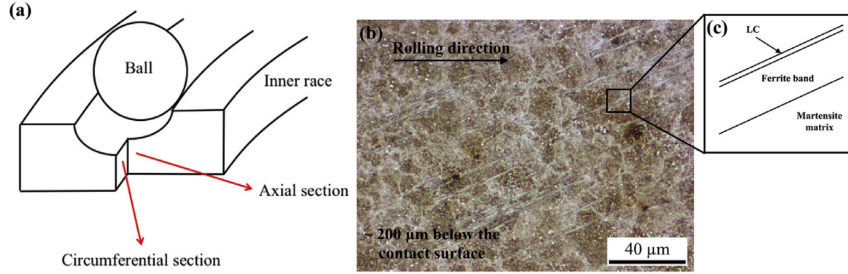


Figure 1: Diagram of DER location within a bearing and its characteristics, taken from [2]. (a) Axial and circumferential sections of a bearing inner ring. (b) Circumferential section of a bearing inner ring under optical microscope, where ferrite bands (white etching bands) are formed in the subsurface. (c) Diagram showing the structure of a WEB consisting of a ferrite band and a LC adjacent to it. One can see the DER region is composed of regions of ferrite interspersed in the parent martensite with lenticular carbides bordering the ferrite bands.

Decay of the martensitic microstructure is complex, with observation of many different phenomena. Martensite transforms to ferrite microbands as a result of strain localization [2, 3, 4, 5, 6, 7, 8, 9, 10]. Residual carbides, untouched at the start of DER formation, gradually dissolve within ferrite and martensite [5, 6, 11]. Further RCF progression leads to the formation of low and high angle ferrite features, White Etching Bands (WEBs), composed of nanocrystalline [7, 11, 12] and elongated ferrite [10]. Lenticular carbides precipitate at the boundaries of these ferrite bands [6, 11]. Thickening of these carbides occurs during DER development and is correlated with WEB growth [2, 13, 14, 15]. Reductions in dislocation density in nanocrystalline (heavily deformed) ferrite have been observed in the later stages of DER formation [1, 16].

Carbon migration is thought to be the mechanism by which this degra-

dation occurs, but it is not definitively known how or where carbon migrates with the onset of DER formation. The key questions are: where does excess carbon from the martensitic matrix find itself when the structure decays to low solubility (0.02 wt%) ferrite? and how is the carbon transported, given its low diffusivity in martensite/DER phases [17]?

Fu *et al.* propose that carbon atoms inside the martensite would segregate to pre-existing/residual carbides, increasing their size [13]. This theory was successfully applied to the growth of lenticular carbides [2], however, problems arise with the application to temper carbide growth: if carbides were to form in martensite, they should follow the Bagaryatskii/Isaichev orientation relationship, but observations suggest a lack of any orientation relationship [18]. Temper carbides residing within DERs have irregular shapes/diffuse boundaries, which are seemingly due to the incomplete dissolution of temper carbides, which is at odds with the theory of Fu *et al.*

A plausible mechanism for carbon migration is that it is driven by dislocation glide, which is as follows [2, 6, 8, 13, 14, 15]. Due to the high dislocation density exhibited in martensite, carbon segregates to dislocations in Cottrell atmospheres, causing pinning. Strain generated by cyclic stresses allow dislocations to escape their carbon rich environment. The free dislocations re-attract carbon, allowing the Cottrell atmospheres to reform, subsequently re-pinning the dislocations, creating a net carbon flux. This mechanism allows for the movement of carbon during the martensite-ferrite transition, while also explaining how excess carbon can move from the ferrite phases to lenticular carbides at the boundaries, describing the process behind both WEB growth and carbide thickening. Moreover, it explains the dissolution of residual carbides, both in ferrite WEBs and martensite, due to dislocation rearrangement and pile ups at the carbide interface drawing carbon atoms out, due to a more favourable binding to dislocations. However, as to how this process occurs on the atomistic scale, or if it is indeed feasible, is unknown.

Experimentally probing dislocation-assisted carbon migration has proven difficult and inconclusive. Work needs to be done to understand dislocation-carbon interactions; more specifically: how dislocations move carbon within the temperature and stress regimes experienced during operation; where carbon is transported to and what the resultant dislocation networks are.

To shed light on this mechanism, a multi-scale modelling approach can be used. Atomistics can provide information of the 2d Peierls energy landscape which dislocations are subject to in iron; and how this landscape is modified by the binding of carbon to dislocations. This data can be used in a line tension model of a dislocation to determine the kink-pair formation energies of dislocations as a function of carbon content and stress. Finally, one can use a kinetic Monte Carlo (kMC) model of dislocation glide by thermally activated kink-pair nucleation, in an environment of carbon. From this last stage of coarse-graining, one can determine in which regimes of tempera-

ture, stress and carbon concentration, dislocation-assisted carbon migration becomes a feasible mechanism behind DER formation, with predictions of dislocation velocity, dislocation configurations and where carbon moves with dislocation glide.

In this report, we will focus on the atomistic portion of this project, directed at understanding dislocation-carbon interactions at the atomistic scale in ferrite (bcc iron). With further knowledge of the fundamental mechanism behind DER formation, we can hope to suppress dislocation motion in the martensitic matrix, mitigating failure by RCF.

2 Computational Method

We use the tight-binding model of Paxton and Elsässer [19], which has been shown to describe the binding energies of carbon complexes in bcc iron, in good agreement with DFT calculations. This model reproduces the two screw dislocation core structures—the easy and hard $1/2\langle 111 \rangle$ cores—exhibited in bcc iron. Study of both is crucial to understanding solute-dislocation interactions. The easy core is the ground state in pure iron, but solutes, such as hydrogen and carbon, have been shown to reconstruct this core into the hard core configuration [20, 21]. Computationally cheaper models, which do not incorporate quantum mechanics, such as the EAM, cannot reproduce these behaviours.

2.1 Peierls Potential

To determine the Peierls potential of the $1/2\langle 111 \rangle$ screw dislocation, we followed the procedure detailed in Itakura [22]. Quadrupolar arrays of dislocations were constructed by placing dislocations of antiparallel $1/2\langle 111 \rangle$ Burgers vectors in an "S" arrangement [23], with initial displacements determined by anisotropic elasticity solutions. See figure 2, left. A quadrupolar arrangement minimises the stress each dislocation experiences in the simulation. These displacements were modified to be periodic, thereby removing artificial stacking faults which would appear between periodic images after introduction of the dislocation dipole. This was achieved by the subtraction of a linear error term from the superposition of displacement fields arising from the dislocations in the simulation cell and its periodic images [24]. To accommodate for the internal stress upon introduction of a dislocation dipole into the simulation cell, an elastic strain was applied to the cell, resulting in an additional tilt component to cell vectors [23, 24]. Simulation cells were constructed with different initial core positions, which were sampled from the triangular region "EHS" (easy, hard and split) core positions, as detailed in figure 3. To fix the dislocation positions during relaxation, the three atoms surrounding the easy core, for each dislocation, were fixed in Z coordinate

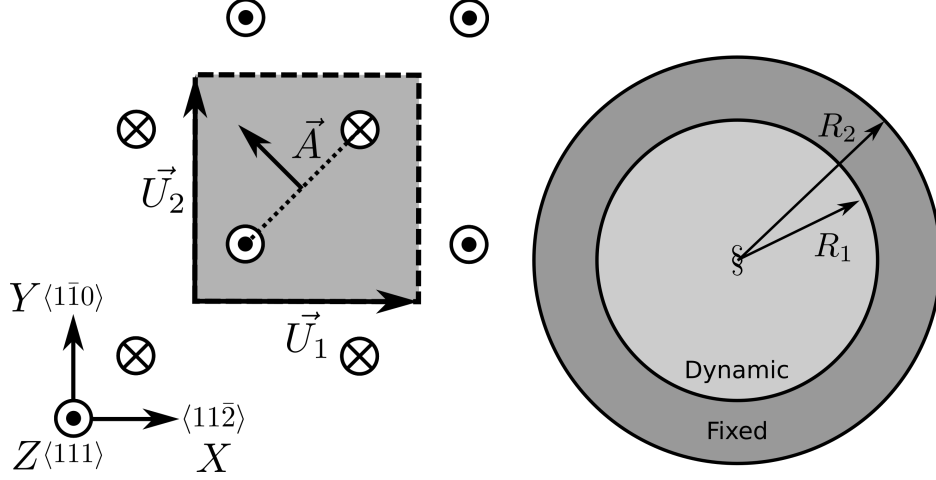


Figure 2: Schematics of dislocation simulation methods. Left: quadrupolar arrangement of dislocations in a simulation cell (grey square). This arrangement minimises the stress experienced by each dislocation in a periodic simulation. Cell vectors \vec{U}_1 and \vec{U}_2 are shown; \vec{A} defines the cut plane between the dipoles. The dislocation positions, and their corresponding burger's vector direction, are denoted by the symbols \otimes and \odot , which are antiparallel to each other. Tilt components added to cell vectors to accomodate for the plastic strain are not shown. Right: cluster method, where atoms are displaced according the displacement field from the screw dislocation at the centre of the cluster, denoted by " \S ". Atoms in the annulus $R_2 - R_1$ are fixed in position to the anisotropic elasticity solutions. Within R_1 , all atoms can relax. Periodicity is only imposed in the Z direction.

during relaxation, where Z is a $\langle 111 \rangle$ direction, along the dislocation line. The k-point sampling mesh for each of these cells was $5 \times 5 \times 30$.

The interaction energy between the dislocation dipole and periodic images was defined differently to Itakura [22]. We followed the prescription of Bulatov and Cai [24] to find a regularised interaction energy, which is independent of truncation limit, in contrast to the formulas quoted in Itakura's papers. Details can be found in section 7.1.

The Peierls potential ΔE_P^i , for an isolated dislocation at the i^{th} core position, can be calculated from

$$\Delta E_P^i = \Delta E_{\text{tbe}}^i - \Delta E_{\text{INT}}^i, \quad (1)$$

where Δ refers to quantities, per dislocation, relative to the relaxed easy core configuration (labelled as E/1, as in figure 3). *e.g.* $\Delta E_{\text{tbe}}^i = \frac{1}{2}(E_{\text{tbe}}^i - E_{\text{tbe}}^{\text{E}})$ is the difference in energy, per dislocation, between a relaxed cell which has the two dislocation cores placed at position i , E_{tbe}^i , and a relaxed cell which has the two cores placed in easy core positions $E_{\text{tbe}}^{\text{E}}$, divided by the

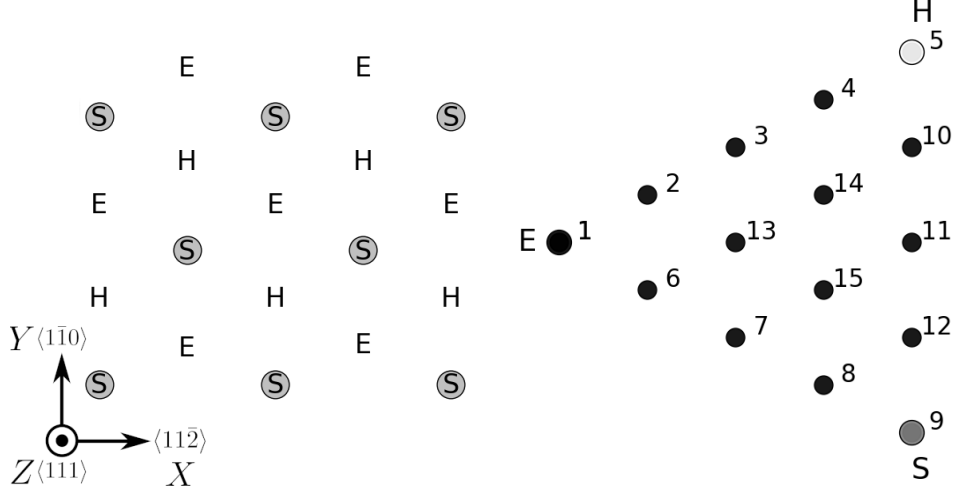


Figure 3: Diagrams of dislocation core positions. "E", "H" and "S" correspond to the easy, hard and split core positions respectively. Left: core positions as seen along the $Z = \langle 111 \rangle$ direction, along the dislocation line. Atomic positions are shown as grey circles. Right: positions sampled within the triangle EHS used to determine the Peierls potential.

number of dislocations in each of the simulation cells. Dislocation-dislocation interaction energies are included in this term, due to dislocations in the simulation cell—and periodic images—interacting with each other, as can be readily seen in figure 2. To model the energy landscape of an isolated dislocation, these interaction energies must be subtracted, which is achieved by the correction term $\Delta E_{\text{INT}}^i = \frac{1}{2}(E_{\text{INT}}^i - E_{\text{INT}}^{\text{E}})$.

2.2 Preliminary calculations

To determine the binding energy of carbon to dislocations, we used the cluster method, as shown in figure 2, right. Simulation cells consisted of a cylindrical cluster of atoms, with a single dislocation introduced into the centre using displacements from anisotropic elasticity solutions. Each of the clusters were centred on the easy or hard core positions. The cluster of atoms was split into two regions: a central region of dynamic atoms with radius R_1 , and an annulus of atoms, between R_1 and R_2 , which were fixed in position to the displacements from anisotropic elasticity.

To confirm the anisotropic elasticity solutions were correct, we compared the displacements against the analytic solutions to the straight screw dislocation, as given in Hirth and Lothe [25]. Furthermore, energy scaling relations were verified. We inserted dislocations into cells of varying radii: $R_1 = x\sqrt{2}a_{\text{bcc}}$, and $R_2 = (x+1)\sqrt{2}a_{\text{bcc}}$, where $x \in \{2 \dots 5\}$. The excess energy was defined as the energy difference of a cell with a dislocation inserted,

E_d , with respect to a perfect cell reference energy of the same geometry,

$$E_{\text{excess}} = E_{\text{core}} + E_{\text{elastic}} = E_d - E_{\text{perfect}}, \quad (2)$$

where $E_{\text{elastic}} = (\mu b^2/4\pi)\ln(R/r_c)$, with $R = R_2$ and $r_c = b$.

Initially, large cells of $R_1 = 6\sqrt{2}a_{\text{bcc}}$, and $R_2 = 7\sqrt{2}a_{\text{bcc}}$ with depth of single burger's vector, were relaxed for both the easy and hard cores, which consisted of 522 and 540 atoms respectively. The three atoms surrounding the core were constrained to only relax in $X-Y$ plane, to fix the dislocation upon relaxation. The k-point sampling mesh for each of these cells was $1 \times 1 \times 24$.

From the relaxed cells, a smaller region of 174 atoms, with $R_1 = 3\sqrt{2}a_{\text{bcc}}$, and $R_2 = 4\sqrt{2}a_{\text{bcc}}$, was cut from the dynamic regions. This smaller cell was extended to a thickness of $3b$ in the Z direction. Carbon interstitials were inserted into octahedral sites near the dislocation core, in the middle layer. Exploiting reflection and rotational symmetry, only 10 interstitial sites needed to be used to obtain the binding energies of carbon ~ 2 b from the core, denoted by iHj and iEj , where $j \in \{1 \dots 10\}$. The final binding sites are denoted by Hk and Ej , where $k \in \{1 \dots 7\}$. The three atoms surrounding the core in the first and third layers were again constrained to relax only in the X and Y directions. No such constraints were imposed on the middle layer.

2.3 Fe-C binding energies

We calculated the carbon-dislocation binding energies as in Itakura [21].

The binding energy is given by

$$E_b = -(E_{d+C} + E_{\text{perfect}} - E_d - E_{C \text{ ref.}}), \quad (3)$$

where E_{d+C} is the total energy of a relaxed cluster with a carbon interstitial and a dislocation, E_d is the total energy of a relaxed cluster with a dislocation and $E_{C \text{ ref.}}$ is the total energy of a relaxed perfect cluster with a single carbon in an octahedral site. A positive binding energy indicates favourable binding.

The zero-point energy (ZPE) is calculated as in Itakura. Details can be found in 7.2. The ZPE corrected binding energy is given by

$$E_b^Z = E_b + \Delta E_z,$$

where $\Delta E_z = E_z - E_z^{\text{C ref.}}$ and $E_z^{\text{C ref.}} = 202.5 \text{ meV}$ is the zero-point energy of carbon situated in an octahedral site in a perfect cluster of the same size.

2.4 Analysis of carbon concentration along dislocation

Using the Fe-C binding energies, one can predict the equilibrium carbon concentration of a carbon binding site c_d , under the assumption that carbon

atoms around the core are sufficiently spaced such that intersite interaction energies are negligible [20].

The concentration is given by

$$\frac{c_d^i}{1 - c_d^i} = \frac{c_{\text{bulk}}}{1 - c_{\text{bulk}}} \exp\left(\frac{E_b^i}{k_B T}\right), \quad (4)$$

where i denotes the i^{th} carbon binding site, with E_b^i , being the corresponding dislocation-solute binding energy (in the convention of attraction denoting a positive binding energy). c_d^i is the average concentration of the i^{th} carbon site bound to the dislocations. c_{bulk} is the carbon concentration in the bulk, with c_{nom} the nominal carbon concentration per Fe atom.

In a given volume V , the number of carbon sites along the dislocation cores is $N_d = \rho V/b$, with ρ the dislocation density, and the number of octahedral sites is $N_{\text{oct}} = 6V/a_{\text{bcc}}$. This imposes constraints on the carbon concentrations: $N_{\text{oct}}c_{\text{bulk}} + N_dc_d = N_{\text{oct}}c_{\text{nom}}/3$, where the factor of 3 is because there are three octahedral sites per Fe atom in the bcc lattice. Using this relation, equation 4 can be solved self-consistently to give the carbon concentration around the core, as a function of nominal carbon concentration and temperature. The nominal carbon concentration was taken to be the maximum solubility of ferrite in the DER region, 0.02 wt% \approx 433 appm [17]. Calculations of 10 and 1000 appm were also performed. The dislocation density was varied between 1×10^{12} , 1×10^{14} and 5×10^{15} , to see the effects of low densities up to the upper bound of dislocation densities $\sim 5 \times 10^{15}$ found in Fe-0.61wt%C martensite [26].

2.5 Line Tension Model

From the atomistic calculations of the Peierls potential and carbon-dislocation binding energies, one can make a line tension model of a dislocation from which we can obtain the kink-pair formation energies as a function of stress and carbon content. This model views the dislocation as an elastic string which moves on the Peierls potential ΔE_P .

The dislocation is modelled as a discretised line, with layer labels j . The energy of the dislocation line is given by:

$$E_{\text{LT}} = \frac{K}{2} \sum_j (\vec{P}_j - \vec{P}_{j+1})^2 + \sum_j \Delta E_P(\vec{P}_j) + (\sigma \cdot \vec{b}) \times \vec{l} \cdot \vec{P}_j - \sum_{j,k} E_C(|\vec{P}_j - \vec{P}_k^C|),$$

where K is a constant calculated from the model, ΔE_P is the Peierls potential, σ is the stress applied and \vec{b} is the burger's vector, with the dislocation line sense given by \vec{l} . \vec{P}_j corresponds to the dislocation core position in a given layer. $E_C(|\vec{P}_j - \vec{P}_k^C|)$ is the binding energy of a particular carbon k , at position \vec{P}_k^C , to a dislocation core positioned at \vec{P}_j . The kink-pair

formation enthalpies can then be found using the string method to relax images which interpolate between the initial and final, to find the height of the transition-state barrier.

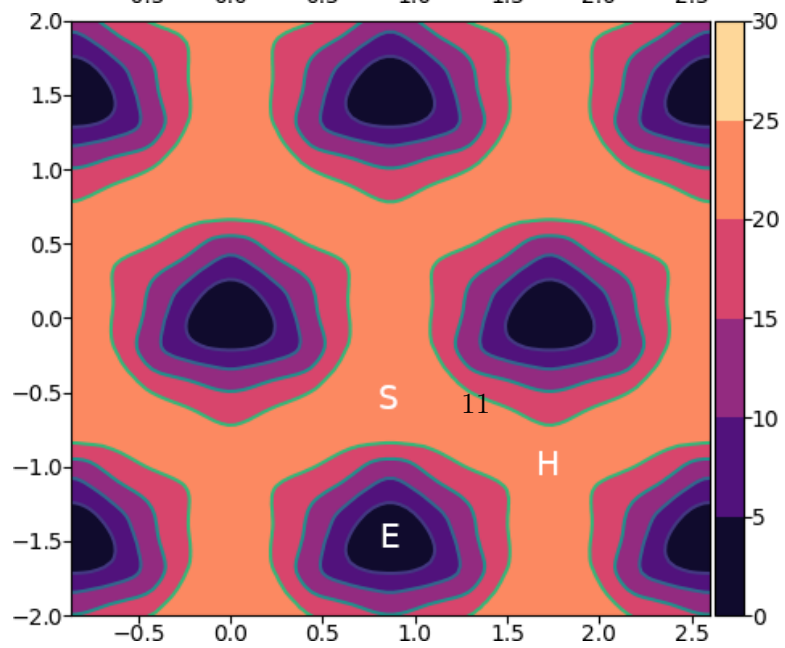
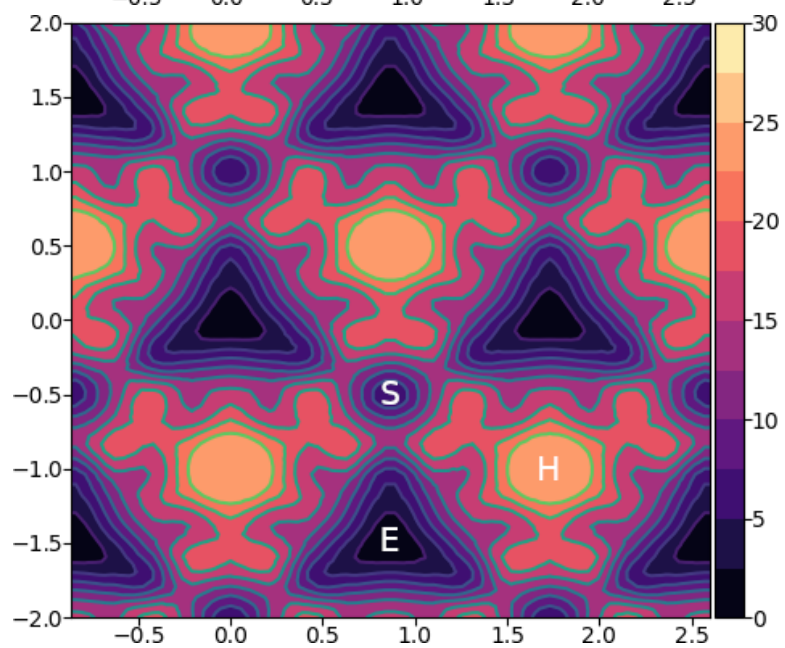
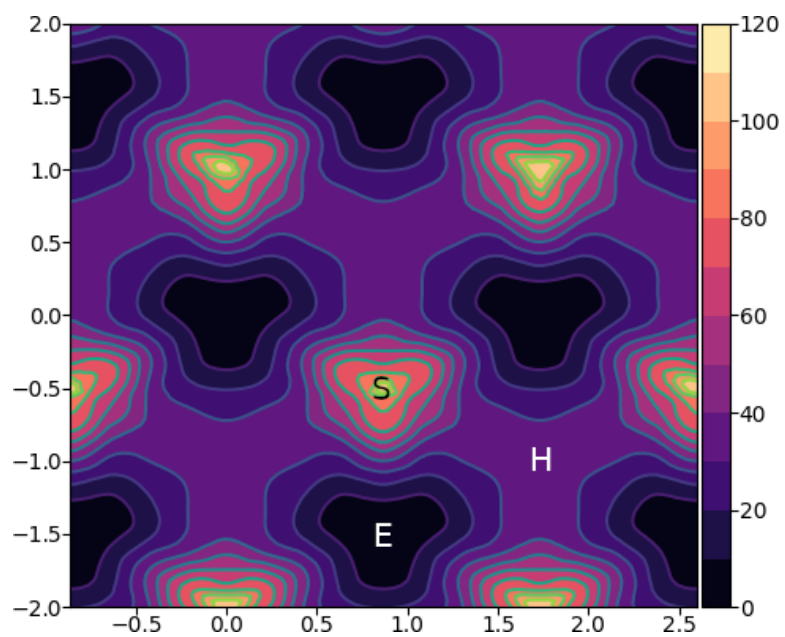
3 Results

3.1 Peierls Potential

Comparison of 2d Peierls potentials of the $1/2\langle 111 \rangle$ screw dislocation between DFT and tight-binding can be found in figure 4, with data found in table 1. The sampled energies were interpolated using 2d cubic splines. The relative energies between the different core positions was found to be smaller in tight-binding compared to DFT. This is an artifact of the model, which has been reproduced in NEB calculations of the $1/2\langle 111 \rangle$ screw dislocation Peierls barrier: the tight-binding Peierls barrier is approximately half that of DFT [27]. The split core energy is lower than that of the hard core, which is reminiscent of EAM potentials [22]. Some of this discrepancy can be attributed to the erroneous interaction term included by Itakura, as detailed above—interaction energies can become arbitrarily high, if not made independent of truncation limit—but likely there are effects in DFT which are not encapsulated fully within the tight-binding description, such as a lack of core electron repulsion upon deformation of the lattice, which would increase the relative energy difference. Consequences of this discrepancy on future kMC simulations are discussed in section 4.

Table 1: Table of energies used to calculate the Peierls potential. All values in meV. $\Delta E_{\text{P}}^{\text{DFT}}$ values taken from [22].

Pos	ΔE_{INT}	ΔE_{tbe}	ΔE_{P}^{sd}	ΔE_{P}^d	$\Delta E_{\text{P}}^{\text{DFT}}$
1	0	0	0	0.0	0
2	-0.7	7.3	7.9	6.3	3.2
3	-1.4	16.0	17.4	15.1	19.2
4	-2.0	22.2	24.2	20.4	31.1
5	-2.5	24.8	27.4	22.6	39.3
6	-3.3	3.0	6.3	4.6	11.5
7	-6.5	7.1	13.6	12.7	39.9
8	-9.6	13.0	22.6	22.7	75.2
9	-12.5	5.4	17.9	26.8	108.9
10	-4.8	22.1	26.9	23.0	34.8
11	-7.2	18.2	25.4	23.5	37.9
12	-9.8	14.0	23.8	24.4	60.7
13	-3.8	11.5	15.3	13.2	17.6
14	-6.9	15.1	22.0	20.3	29.9
15	-4.3	18.6	22.9	20.0	39.7



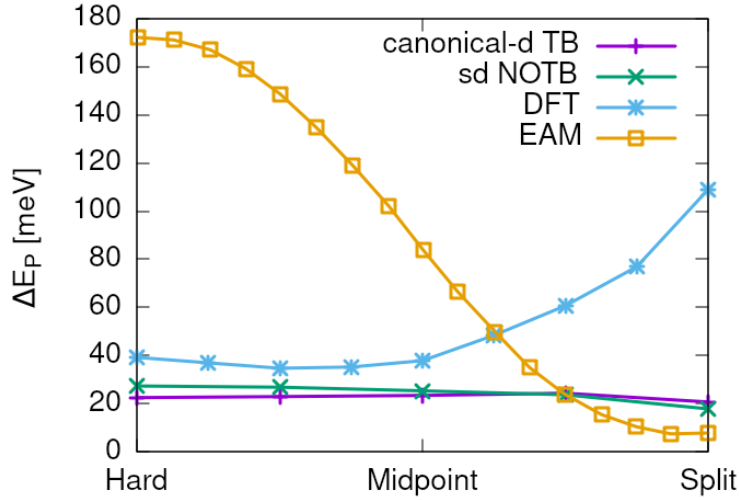


Figure 5: Peierls potential along the hard-split line. One can see in *s-d* tight-binding model is similar to the EAM potential of Mendelev [28]: it decreases constantly from the hard core to the split core, which will result in a kink shape which goes through the split core position. In DFT one finds a saddle point between the hard core and the midpoint, in which a kink in the transitional state will go through.

The expected transitional kink shape from this Peierls potential may differ compared to DFT, with dislocation core positions possibly being situated closer to/at the split core position, similar to EAM potentials [22]. Following the Peierls potential along the H-S direction, figure 5, we see that the Itakura potential has a saddle point, whereas in *s-d* tight-binding there is not: the Peierls potential decreases monotonically from the hard core to the split core position. However, calculation of the Peierls barrier between two easy core positions in the canonical *d*-band version of this tight-binding model (where *s-d* hybridisation and non-orthogonality are simply turned off) found core positions of the transitional kink state to go through the metastable point, similar to DFT [27]. Furthermore, the canonical *d*-band model produces structural energy differences and elastic constants which are closer to values in literature than the *s-d* model [29]; as such, it could provide a better description of Fe-Fe interactions, and the Peierls potential, by extension. To verify this, recalculation of the Peierls potential using the canonical model will need to be undertaken.

The Peierls potential with the *d*-band model was found to be more reminiscent of DFT (with these specific contour bounds); but the difference is small: the maximum difference between the *s-d* models is ~ 10 meV, with an average difference of $\sim +3$ meV to the former.

Along the hard-split line, instead of monotonically decreasing, like the

s - d model, there is an increase in energy from the hard core up until close to the midpoint, at which it decreases to the split core energy. Previous calculations of the Peierls barrier of the d -band found that the peak of the Peierls barrier was close to the midpoint, as in DFT, see figure 6.

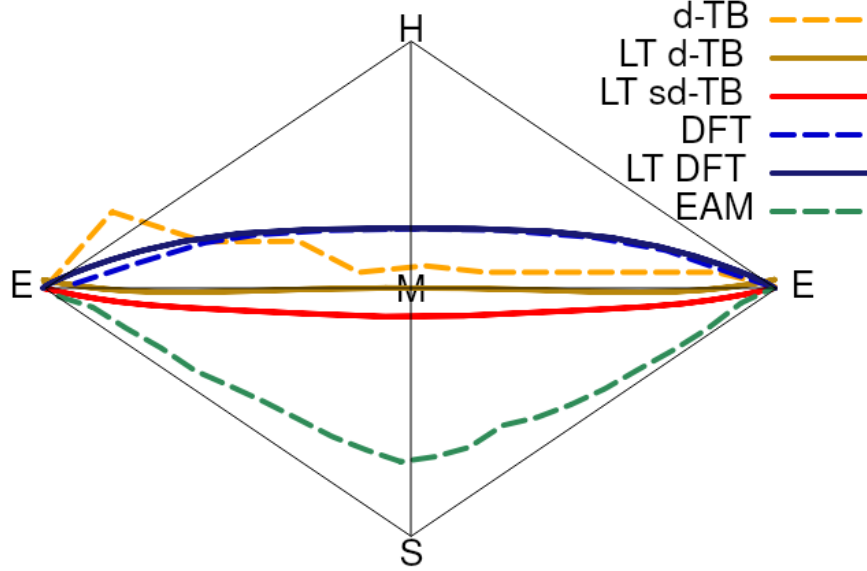


Figure 6: Comparison of the Peierls potentials (left) produced from d -band tight-binding, DFT and EAM along each of their respective minimum energy pathways (right), which are the reaction coordinates for the figure on the right. The EAM potential of Mendelev [28] has an unphysical well in the centre of the potential, while tight-binding and DFT produce single-humped potentials. Tight-binding follows a pathway much closer to that of DFT. EAM potentials predict that the dislocation core goes to the split core and then back to the easy core. Even though the Peierls landscape found in tight binding has similar characteristics to the EAM in terms of the energetic ordering of different core states, the description of the minimum energy pathway of the $1/2\langle 111 \rangle$ screw dislocation as it moves between core positions is in good agreement with DFT.

In the EAM model, the midpoint along the hard-split transition is not a saddle point. The MEP for kink-pair formation deviates widely from the DFT path.

3.2 Preliminary calculations

To validate the cluster simulation method, the excess energy, defined as the difference in energy between a cell with a dislocation, and a perfect reference cell, was plotted as a function of $\ln(R/r_c)$, where $R = R_2$ of the cluster and $r_c = b$, as seen in figure 7. In isotropic elasticity theory, this should give a linear dependence where the gradient corresponds to $\mu b^2/4\pi$, with the y intercept corresponding to the core energy E_{core} . This is well reproduced by our model, except at low $\ln(R/r_c)$ as expected, where the cell size is not large enough to accommodate for sufficient relaxation of the dislocation core, increasing the core energy, which is not accounted for in elasticity theory.

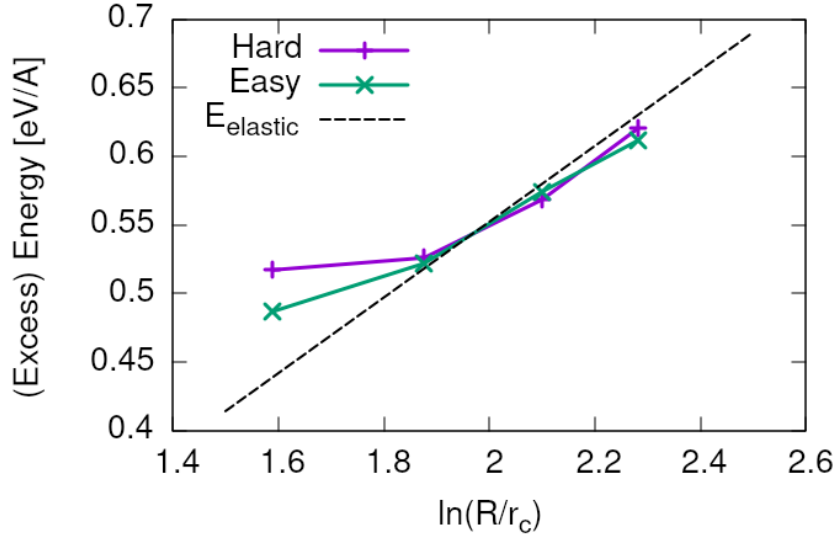


Figure 7: Excess energy of dislocation clusters with differing radii for both the easy and hard core configurations. The prediction from elasticity theory is given by the black, dashed line. Deviation of both cores occur when cell size is small, creating an increase in the core energy, which elasticity theory cannot account for.

The energy cost to transform from the easy to the hard core can be estimated by the difference in excess energies between the cores in the limit of $\ln(\frac{R}{R_0}) \rightarrow 0$. At the smallest measured value, one finds that the core energy difference $\Delta E_{\text{core}}^{\text{Easy-Hard}} = 76 \text{ meV/b}$, which is in good agreement with the DFT value of 82 meV/b [22].

For a line tension model of a dislocation, it is necessary to ascertain the energy, denoted $E_L = E_{\text{el}} + E_{\text{core}}$ as in Provile [30]. This can be obtained by subtracting the total energies of relaxed dislocation configurations to obtain the core energy.

3.3 Fe-C binding energies

As found in DFT simulations by Ventelon [20], when a carbon was placed in the vicinity of a relaxed easy dislocation core—in either of the two nearest, distinguishable, octahedral sites—a spontaneous reconstruction of the dislocation core occurred: from easy to hard. Upon reconstruction, the dislocation core moved to a neighbouring triangle, when looking along the $\langle 111 \rangle$ direction, where the carbon found itself situated in the centre. This will be called a prismatic site, as in Ventelon’s paper. This confirms that both hard and easy dislocation cores must be studied to fully understand screw dislocation behaviour in bcc iron.

The binding energies of carbon to both the hard and easy cores can be seen in table 3, with the resulting distribution of carbon in figures 8 and 9. The distribution of carbon strongly depends on the type of core it finds itself situated near. The easy core only significantly modifies the position of the iE1 site, to the E1 site, situated in the centre of an adjacent triangle. All other sites are unaffected, so there is a one-to-one correspondence between all iE j and E j sites, where $j \in \{2 \dots 10\}$. There are carbon basins available close to the triangular region containing the core, but not inside.

Carbon favours a prismatic site within the hard core (H1), which has the highest binding energy, 1.29 eV, of all sites considered. There are no binding sites apparent in a triangular annulus (of width $a_{\text{bcc}}\sqrt{2}/2$) surrounding the hard core triangle due to the destruction/volume reduction of octahedral sites near the hard core. The initial octahedral sites, iH1 and iH2 decay to the H1 site. Similarly, iH3 and iH4 decay to the H2 site, with iH9 and iH10 decaying to a H7 site. Relations between each of the sites is given in table 2.

Table 2: Decay relations between the initial and final sites upon relaxation of carbon interstitials around the hard core.

Initial	Final
iH1, iH2	H1
iH3, iH4	H2
iH5	H3
iH6	H4
iH7	H5
iH8	H6
iH9, iH10	H7

Note that interactions between carbon atoms around the core are not taken into account here: figures 8 and 9 are purely diagrammatic and not what one expects the true distribution of carbon around a screw dislocation would be. Carbon is strongly repulsive at first nearest-neighbour distances, which would modify each of these distributions.

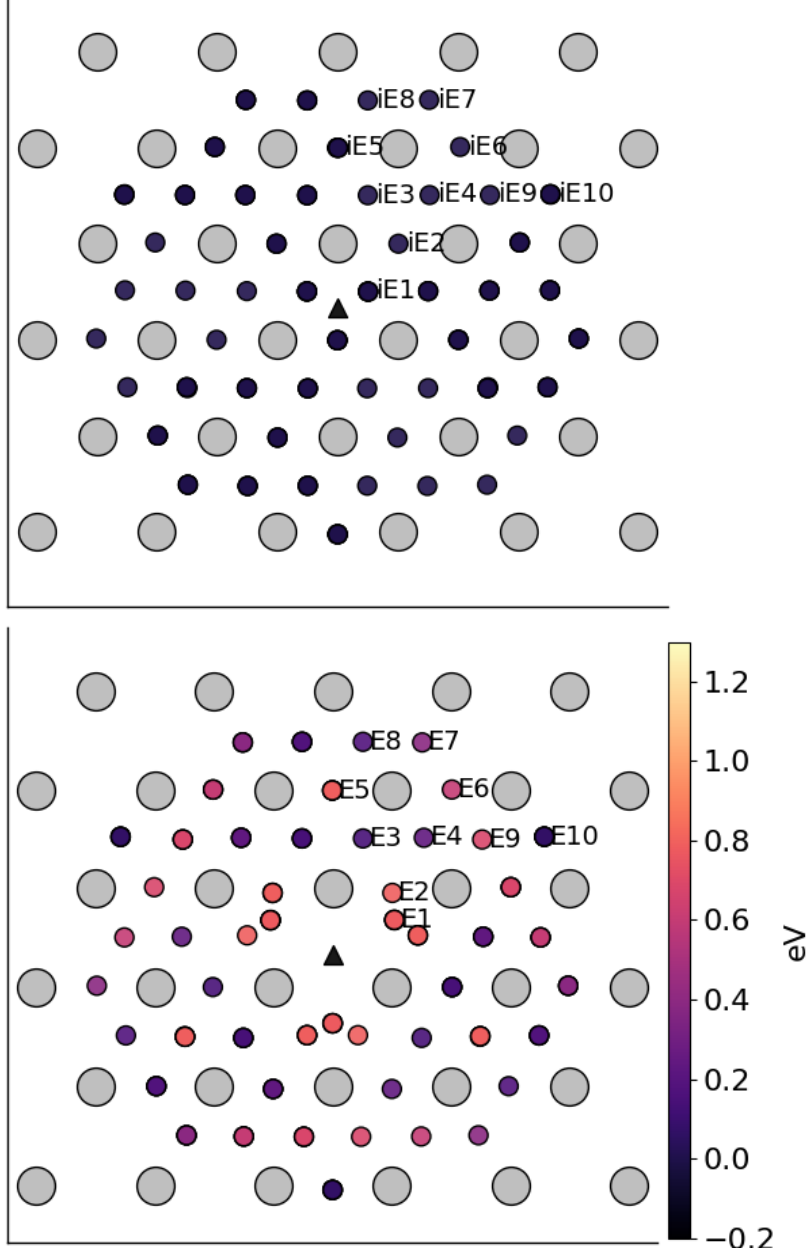


Figure 8: Initial (top) and final (bottom) positions and binding energies (eV) of carbon around the easy core. Binding energies are not shown for the initial positions. Top: initial positions before relaxation. Bottom: final positions and binding energies after relaxation. The core was constrained by fixing the top and bottom three atoms surrounding each of the cores. As shown by Ventelon [20], the first and second closest octahedral sites to the hard core decay to a prismatic position inside the hard core.

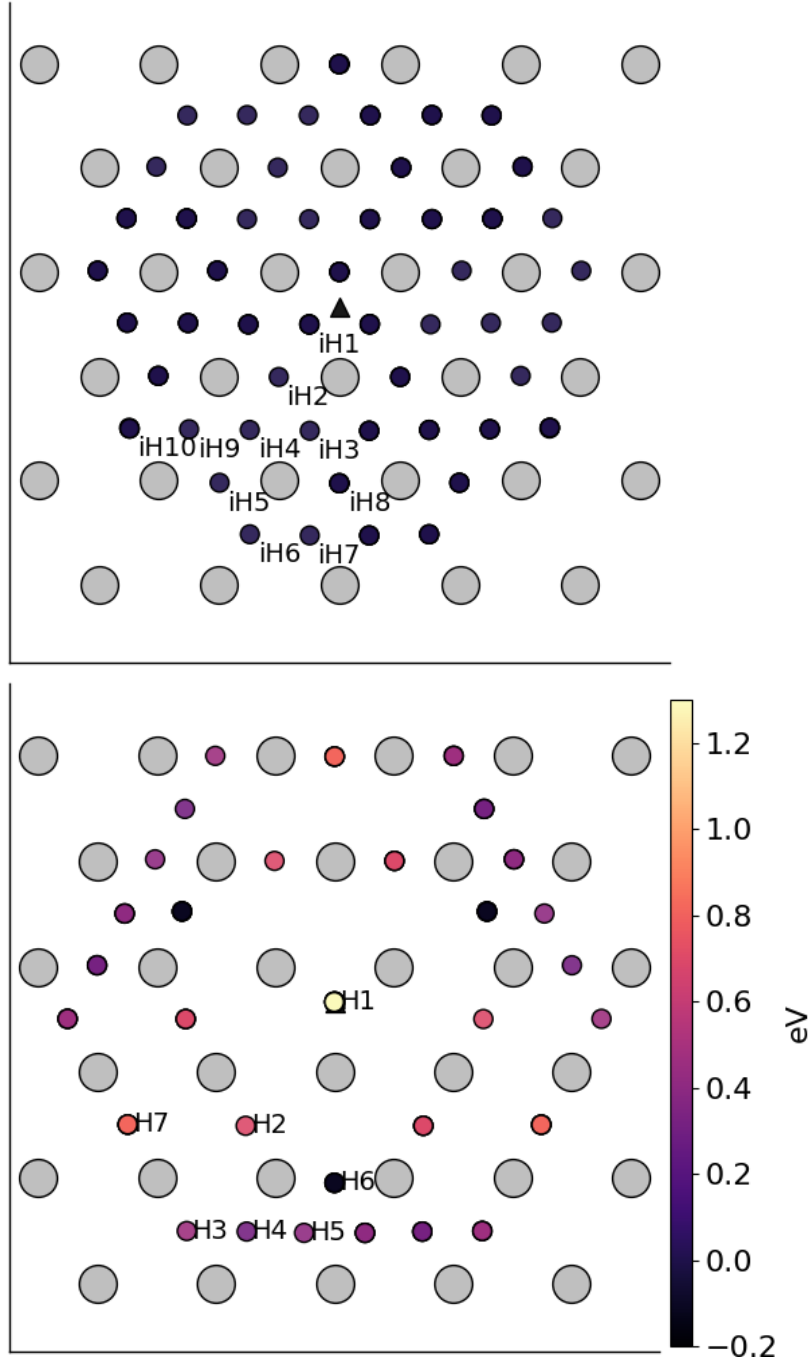


Figure 9: Initial (top) and final (bottom) positions and binding energies (eV) of carbon around the hard core. The core was constrained by fixing the three atoms surrounding each of the cores in the top and bottom layers. As shown by Ventelon [20], the first and second closest octahedral sites to the hard core decay to a prismatic position inside the hard core.

Site Type	distance from core [b]	E^z [eV]	ΔE^z [eV]	E_b [eV]	E_b^z [eV]
E1	0.57	0.185	-0.018	0.793	0.775
E2	0.70	0.202	-0.001	0.793	0.793
E3	0.99	0.205	0.002	0.137	0.139
E4	1.21	0.208	0.005	0.229	0.234
E5	1.36	0.210	0.008	0.784	0.791
E6	1.66	0.209	0.007	0.597	0.603
E7	1.89	0.206	0.003	0.385	0.388
E8	1.77	0.203	0.000	0.177	0.178
E9	1.52	0.201	0.000	0.683	0.683
E10	1.95	0.202	0.000	0.067	0.067
H1	0.00	0.196	-0.006	1.298	1.291 [0.881 ^a , 0.790 ^b]
H2	1.19	0.210	0.007	0.691	
H3	2.12	0.209	0.007	0.461	
H4	1.91	0.207	0.005	0.311	
H5	1.80	0.208	0.006	0.403	
H6	1.40	0.207	0.005	-0.119	
H7	1.35	0.206	0.006	0.825	

Table 3: Table of energies leading to the zero-point energy corrected binding energy using the cluster method for simulation of dislocation-carbon interactions. ^a Tight-binding quadrupolar array results, starting from a fully relaxed easy core quadrupole extended to a depth of 3b with carbon introduced into the iH1 site in the middle layer, by both dislocations. ^b DFT results of Ventelon, using the same quadrupolar configuration as in ^a. In both quadrupolar simulations, carbon ended up in the H1 site.

These binding energies agree well with experiment and atomistic/elastic calculations. EAM simulations by Clouet [31, 32] found a maximum binding energy of 0.41 eV by calculating the elastic dipole tensor within Eshelby theory. Hanlunmyuang *et al.* [33], similarly conducted DFT and EAM calculations for the interaction energy 12 Å from the core, and their calculations agreed with the continuum limit of Eshelby theory with a binding energy of 0.2 eV. In DFT calculations by Ventelon [20], the interaction energy of a carbon in a hard core prism configuration was found to be 0.79 eV for a thickness in the Z direction of $3b$ (0.73 eV for $6b$)—in the convention that a positive binding energy indicates attraction. This is significantly lower than the 1.29 eV interaction energy of tight-binding. This discrepancy can be partially explained by the fact that the cells have not been allowed to relax with all degrees of freedom, as in the Ventelon results: the three atoms around the screw core are fixed in Z so the dislocation core position does not change upon relaxation.

Repeating the calculation for the binding of a H1 carbon to a screw dislocation using a quadrupolar array, allowing for all atoms to relax, gives a binding energy of 0.88 eV. This agrees very well with the DFT results of Ventelon [20].

A source of error for this discrepancy is likely from the fitting of the tight-binding model itself. The Peierls barrier of this s - d model of iron, necessary for Fe-C interactions, has been shown to be half that found in DFT [27], but the solution energies for Fe-C defect complexes are well described. This implies there is insufficient repulsion between Fe-Fe species upon deformation, leading to a larger resultant Fe-C binding energy from tight-binding.

3.4 Analysis of carbon concentration along dislocation

Variation of carbon concentration along the dislocation line for each of the binding sites can be seen in figure 10. Due to the lower overall binding energies of carbon to the easy core, the concentration of weakly bound sites occurred at a lower temperature. Dislocation densities near the upper bound of what has been observed in martensite, $\rho \approx 10^{15}$, reduce the temperature at which carbon concentration decreases around the dislocation core. Lower nominal carbon concentrations cause carbon concentrations around the dislocation to decrease at a lower temperature.

In the operating temperature range of 40–90 deg C = 310–360 deg K, we expect most hard core sites are saturated. Given the high concentrations of the E1/E2 sites around the easy core in this range, we expect all dislocations will be of the hard core type, due to reconstruction of the easy core by the adjacent carbon.

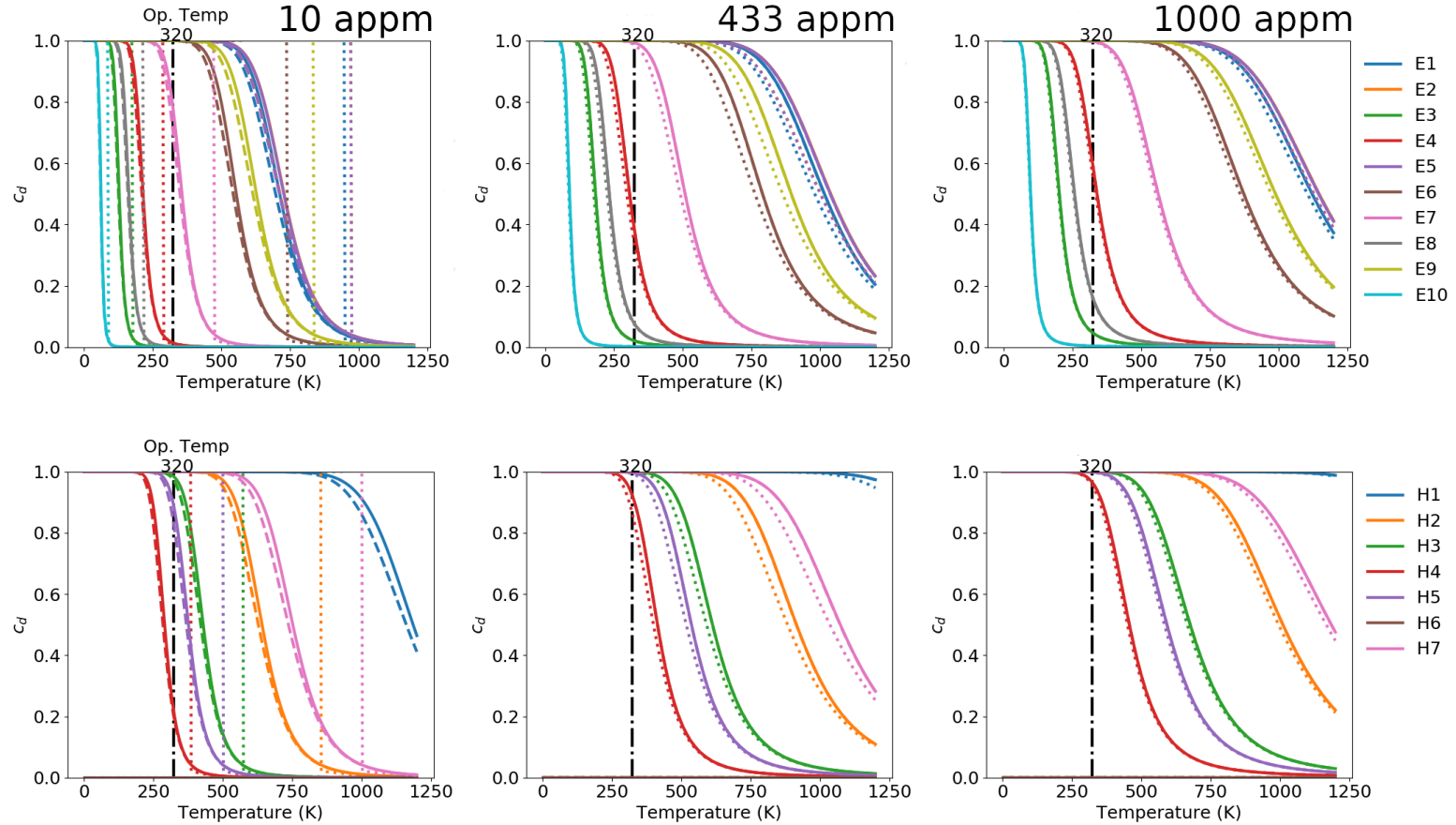


Figure 10: Variation of carbon concentration on the dislocation line c_d for each of the binding sites for the easy core (top) and hard core (bottom). Solid, dashed and dotted lined correspond to dislocation densities of 1×10^{12} , 1×10^{14} and 5×10^{15} respectively. The nominal carbon concentrations are 10 appm (left) and 1000 appm (right), with the middle figures taken to be the concentration of carbon at the solubility limit C in ferrite: $0.02\text{wt}\% \approx 433$ appm. c_d and c_{bulk} reached self-consistency, with an absolute tolerance of 1×10^{-3} . C-C interactions were not taken into account. The concentration of carbon around the easy core, drops off at a lower temperature than that of the hard core due to lower binding energies, with reduction in concentration. The operating temperature is taken to be $50 \text{ deg C} = 320 \text{ deg K}$.

3.5 Progression to Line Tension Model

The K coefficient for the line tension model was calculated from atomistic simulations, using the method of Itakura [22], by calculation of a Hessian from the displacement of atoms surrounding the dislocation core. Tight-binding gave $K = 0.734 \text{ eV}\text{\AA}^{-2}$, which agrees well with DFT, where $K = 0.816 \text{ eV}\text{\AA}^{-2}$.

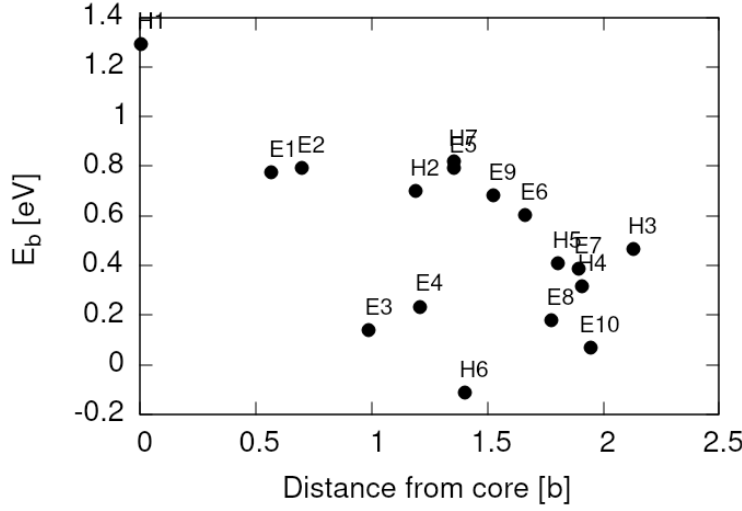


Figure 11: Distance dependence of the binding energies of carbon to the $1/2\langle 111 \rangle$ screw dislocation in iron. Positive binding energies denote a favourable binding.

Dislocation-carbon binding energies were found to decay with distance, as seen in figures 11 and 12. A Lorentzian was fit to specific binding energies such that a continuous function could be used to describe binding within the line tension model. This is a purely empirical model. The choice of sites used for the fitting is discussed in section 4.

A julia implementation of the string algorithm, accelerated by use of an ODE solver, was used to relax the images [34]. One finds that the line shapes are similar to that of Itakura, for the x-coordinate of the dislocation core position.

The kink width in tight-binding is slightly wider than that found in DFT, which corresponds with the fact that the width is proportional to $b\sqrt{K/\Delta E_P^{\text{tbe}}}$, where the reduction in ΔE_P^{tbe} is greater than the reduction in K^{tbe} [22].

To validate the model, the itakura dat

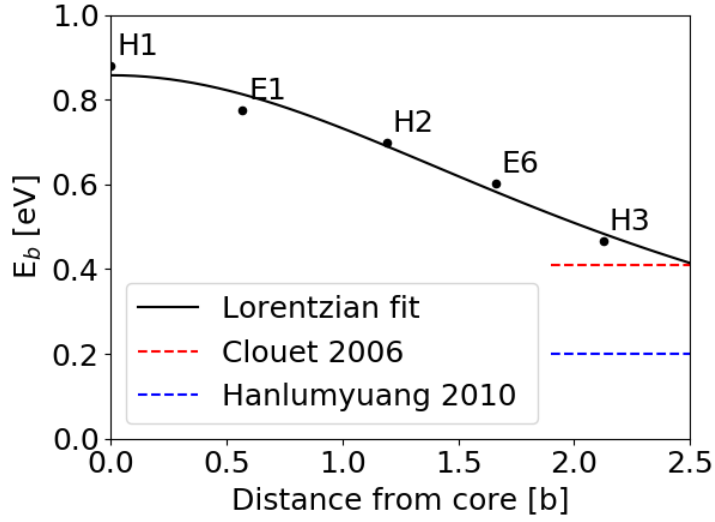


Figure 12: Fit of Lorentzian to carbon-dislocation binding energies. The sites chosen to fit to were determined by those sites a prismatic carbon in a hard core configuration would find itself, if the dislocation were to move without it along the $X = \langle \bar{2}11 \rangle$ direction.

Table 4: Kink-pair formation energies between DFT, and the two flavours of tight-binding used with the line-tension model.

Method	$E_{\text{kp}}^{\text{form}}$
DFT	0.71 eV
TB (sd-non-orthog.)	0.56 eV
TB (d-orthog.)	0.53 eV

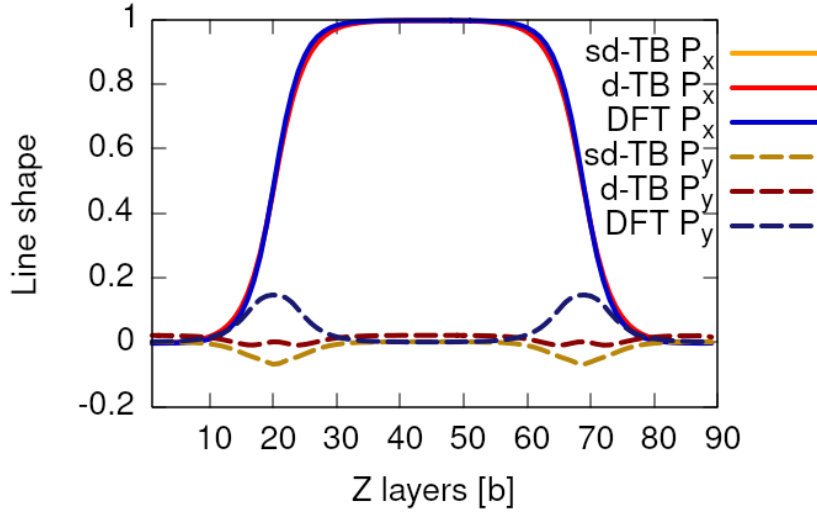
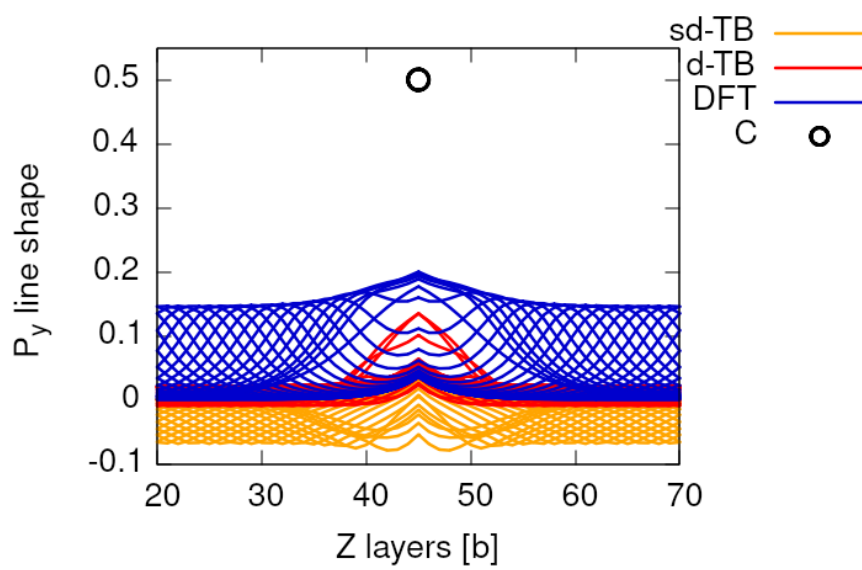
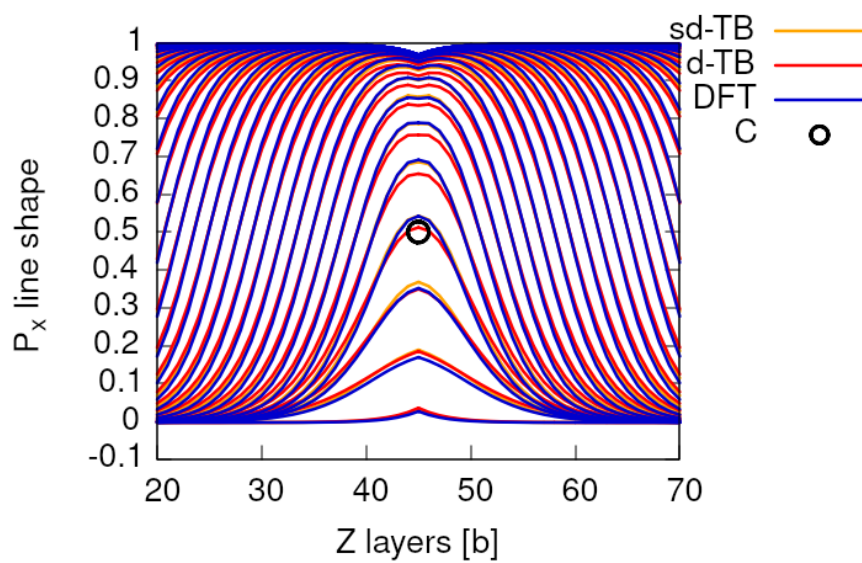
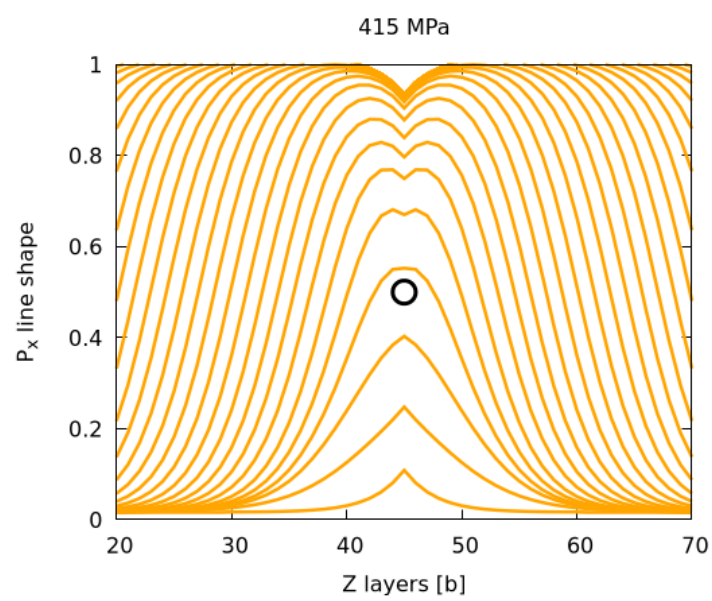
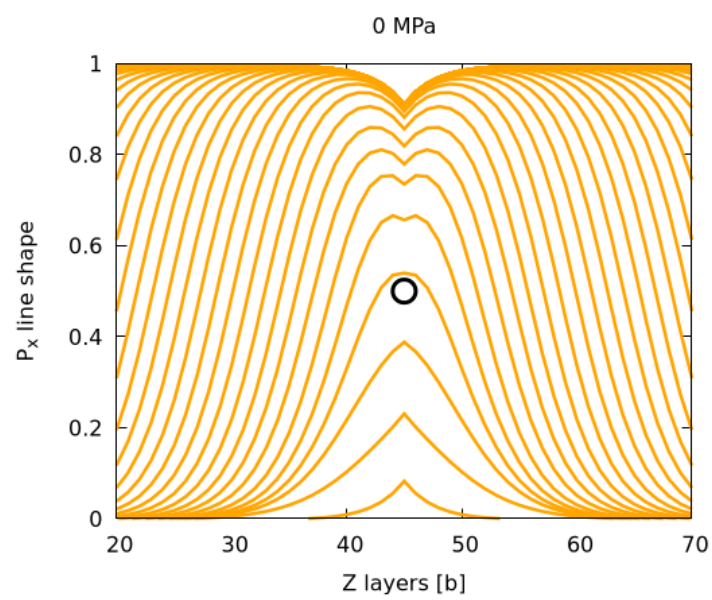


Figure 13: Core positions of the line tension model from DFT (blue) and tight-binding (yellow) for the middle image corresponding the MEP and the kink-pair formation energy. Images were relaxed using the ODE String method of Makri and Ortner [34]. P_x and P_y correspond to the x/y-coordinate of the dislocation core position in each of the discretised layers of the dislocation. One finds that the kink width in tight-binding is wider than that found in DFT, which corresponds with the fact that the width is proportional to $b\sqrt{K/\Delta E_P}$, where the reduction in ΔE_P^{tbe} is greater than the reduction in K_{tbe} .





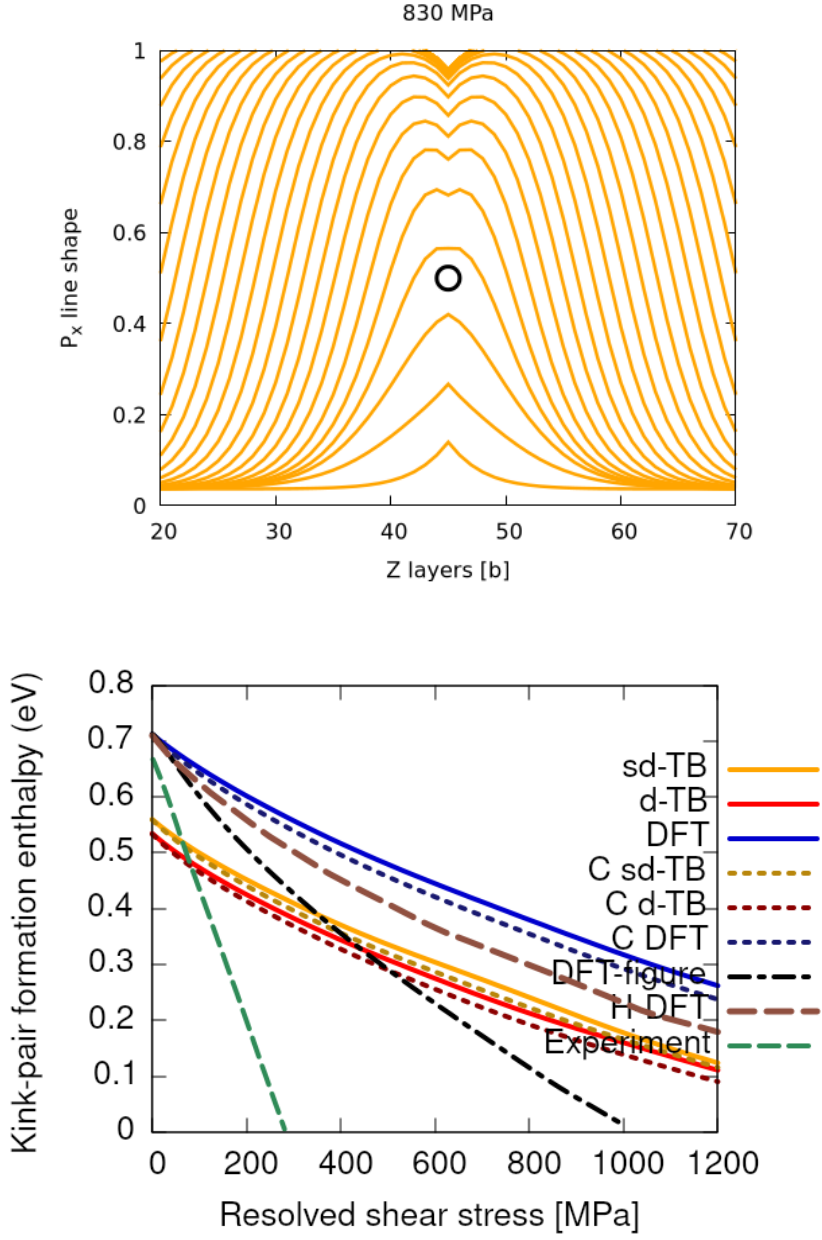
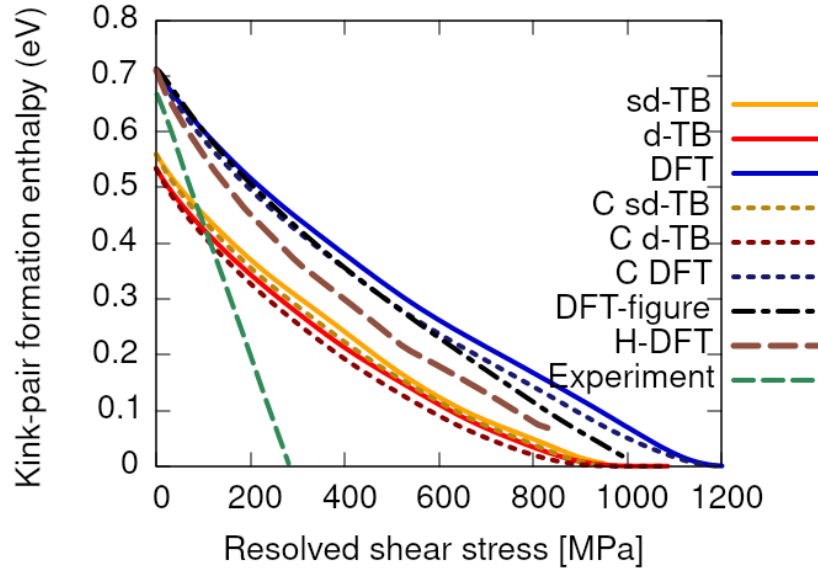


Figure 14: Dependence of the kink-pair formation enthalpy with increasing stress on the $[111](1\bar{1}0)$ direction. DFT results taken from Itakura [22], with experimental data taken from Spitzig [35] .



Analysing the energies given at each point of the image in the transition state, one can find the Peierls potential. Each of the Peierls potentials from these calculations match well with atomistic NEB simulations from both DFT and tight-binding [36, 27].

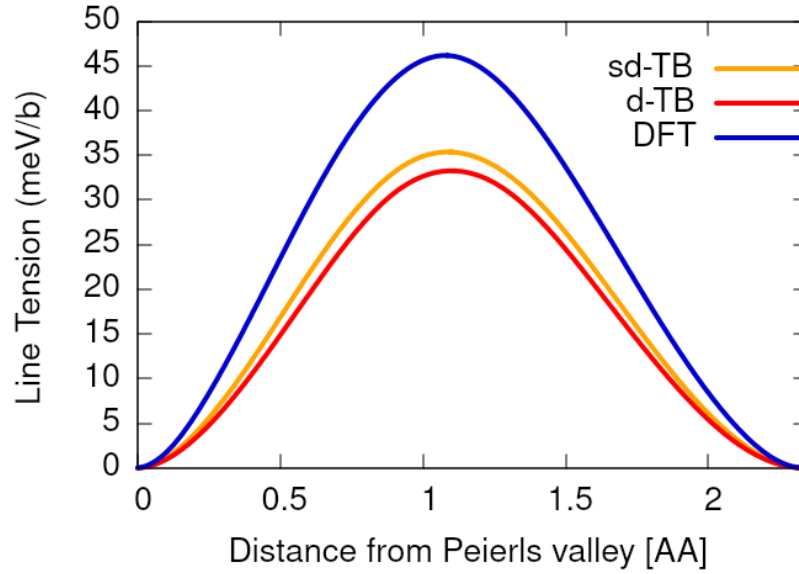


Figure 15: Peierls potential obtained with line tension model from the Itakura data set and tight-binding simulations. The height of these barriers agree well with atomistic NEB calculations of the Peierls barrier in both DFT and tight-binding.

4 Discussion

We expect a reduction in the kink-pair formation enthalpy in tight-binding, due to the slightly smaller overall Peierls potential along the expected minimum enthalpy path of the kink within the line tension model. This would increase the rate of kink nucleation in kMC models, causing a higher overall dislocation velocity. This will increase the disparity between the dislocation velocity and the speed of carbon diffusion. In the vicinity of the dislocation line, there is a "high-mobility" zone for carbon to diffuse easily around the dislocation [37]. Assuming a similar kink shape as found in DFT calculations, we expect the kink-pair formation energy to be ~ 0.7 eV, which is similar in magnitude to the DFT value (0.73 eV) [22]. Hence, we predict the increase in dislocation velocity would not be so large as to effectively negate the effect of the high-mobility zone—which would result in carbon not being able to "catch-up" to dislocations upon movement. Therefore, we do not expect the observed discrepancy in the Peierls potential to significantly change the principal mechanisms observed, or results obtained, from kMC simulations of dislocation-assisted carbon migration.

As in Lüthi [38], carbon interactions were found to be vital in understanding how screw dislocations move in steels, due to the spontaneous reconstruction of the pure iron ground state (easy core) upon introduction of carbon. From the large binding energy of the H1 site, one would expect a hard core with carbon in a prismatic site as the ground state configuration for pinned dislocations.

In the context of dislocation-assisted carbon migration, with sufficient contact stress, dislocations in their hard core ground state will be forced to move (say, along the $X = \langle \bar{2}11 \rangle$ direction), which results in the hard core reconstructing to an easy core. Due to the much higher velocity of dislocations, relative to the diffusivity of carbon, the prismatic carbon will stay in-place, becoming an E1 site. A drag force now acts to impede motion of the dislocation, due to the binding of the carbon in the E1 site. Progression of dislocation glide results in further reconstruction of the dislocation core to hard and easy states, with the original carbon being situated in H2, E6 and H3 sites, relative to the dislocation centre. Thus as the dislocation moves, there is a significant drag force acting on the dislocation, which decreases the further the dislocation moves from carbon, as one would expect. This suggests that a dislocation-assisted carbon migration mechanism could be feasible, but the last two stages of the multi-scale model are necessary to verify this.

In normal operating temperatures of the bearing, one expects all dislocations to be hard cores saturated with carbon (neglecting C-C interaction) in most of the H j sites, as seen in the concentration analysis. In ferrite that has just transformed, assuming a C concentration of 0.6 wt% as seen in martensite, we expect similar behaviour to the 1000 appm case as seen in

figure 10. Including C-C interactions would reduce these concentrations from saturation. There is insufficient data to say how strong this effect would be.

5 Future work

The prerequisites for a line tension model are in place for determination of the kink-pair formation enthalpies of screw dislocations as a function of carbon content and stress. This is ongoing work. Validation tests will be carried out on the Itakura data set for the binding of hydrogen to screw dislocations in bcc iron.

Using the kink-pair formation enthalpies and the binding energies of carbon to screw dislocations, one can proceed with kinetic Monte Carlo simulation of dislocation glide, in an environment of carbon to understand how dislocations move carbon under applied stress, in different temperature and nominal carbon concentration regimes.

It would be of interest to pursue atomistic calculations of carbon bound to edge dislocations. Recent DFT/Eshelby theory calculations by Maugis *et al.* [39], show under *compressive* stress, carbon diffusivity is *enhanced*. Pipe diffusion along edge dislocations could therefore be an important aspect to consider in carbon transport, in addition to the higher mobility of edge dislocations in bcc iron. As such, edge dislocations could be quite important within the mechanism of dislocation-assisted carbon migration.

Ising and Monte Carlo models of intersite carbon interactions have been performed using the results of DFT carbon-dislocation binding energies [38]. These calculations only considered the hard core, with carbon binding sites of the H1 prismatic site and a H2 site, (which they name P and $O^{(4)}$ respectively). First neighbour C-C interactions were taken into account, both along the dislocation line and between carbon sites. Using the tight-binding calculations detailed in this report, we can easily apply and extend this analysis to consider more binding sites around the hard core, and observe stable carbon distributions around the easy core.

Analysis of carbon diffusion barriers around a dislocation are necessary. In a DFT/EAM study of carbon-supersaturated ferrite in pearlitic wires, it was found that carbon can diffuse easily around the dislocation, which is an important consideration in the drag mechanism proposed [37].

6 Conclusion

Dislocation-assisted carbon migration is thought to be a viable mechanism by which martensite decays to form DER regions—mostly composed of ferrite interspersed in a martensitic matrix—which enhances failure risk by RCF. There is dispute over where excess carbon from the martensitic matrix finds itself upon transformation to ferrite, of much lower carbon solubility.

The current leading mechanism suggests carbon segregates to pre-existing carbides, yet experimental results show in the late stages of DER formation, pre-existing carbides are partially dissolved in areas of highly localized plasticity, implying segregation of carbon to dislocations. As such, a thorough investigation of carbon-dislocation interactions is vital to understanding how DER initially forms and progresses.

Atomistic calculations using tight-binding, the first stage in a multi-scale paradigm to understand dislocation-assisted carbon migration, found a Peierls potential with characteristics comparable to both EAM/DFT results. A canonical d -band model may better describe this energy landscape. It is not expected that the discrepancy in the Peierls potential would significantly change results in kMC simulations.

Carbon distribution around the easy and hard cores were found to differ significantly, with the largest binding energy being found by carbon being situated in a prismatic site in the hard core. Carbon within 3\AA of the easy core caused reconstruction to the hard core, with carbon in a prismatic site.

Equilibrium concentrations of carbon around the hard/easy cores at normal operating temperatures suggest that all dislocations are of hard core type with carbon situated in a H1/prismatic site, with reconstruction of all easy core dislocations to hard core, resulting in all dislocations being pinned.

If a dislocation moves under stress from the hard core-prismatic carbon ground state, a large drag force acts on the dislocation upon movement to adjacent easy and hard positions, assuming the carbon will stay in place due to its low diffusion coefficient, relative to dislocation velocity. The carbon-dislocation binding energies decrease with distance, and are in good agreement with literature. This suggests that a dislocation-assisted carbon migration mechanism is plausible, but more work needs to be done to confirm if so.

Further work will be done to ascertain diffusion barriers around the dislocation, which have been shown to be significantly reduced from bulk values due to the presence of dislocations in DFT/EAM calculations [37]. This will complete the description of the solute drag mechanism.

Line tension and kMC models will be used to determine how dislocation glide is affected by carbon and how carbon can move with dislocations.

7 Appendix

7.1 Regularisation of interaction energy in quadrupolar array

In isotropic elasticity, the elastic energy of a single dislocation dipole in an infinite lattice is given by

$$E_{\text{el}}^{\infty} = \frac{\mu b^2}{4\pi} \ln\left(\frac{r}{r_c}\right)$$

The contribution from periodic images to the correction is

$$E_{\text{img}} = E_{\text{el}}(\mathbf{a}, \mathbf{c}_i, r_c) - E_{\text{el}}^{\infty}(\mathbf{a}, r_c),$$

"Ghost" dipoles are introduced to account for the conditional convergence of the sum at $\pm\alpha\mathbf{b}$ and $\pm\beta\mathbf{b}$, where $\alpha = \beta = 0.5$. We define $E_{\text{dg}}(\mathbf{R})$ as the interaction energy of a ghost dislocation and a dipole at \mathbf{R} anisotropic elasticity equations as shown in [40].

Defining,

$$E_{\text{dd}}(\mathbf{R}) = \frac{\mu b^2}{2\pi} \ln \frac{|\mathbf{R}|^2}{|\mathbf{R} + \mathbf{a}| \cdot |\mathbf{R} - \mathbf{a}|},$$

we obtain,

$$E_{\text{img}} = \frac{1}{2} \sum_{\mathbf{R}} [E_{\text{dd}}(\mathbf{R}) - E_{\text{dg}}(\mathbf{R})] - \frac{1}{2} E_{\text{dg}}(\mathbf{R} = 0),$$

which can be subtracted from the total energy as given from atomistic calculations, for a regularised interaction energy.

7.2 Zero-point energy calculation

After relaxation of the C-dislocation system, a 3x3 Hessian matrix is constructed by taking the numerical derivative of forces observed on the carbon atom after displacement by ± 0.015 in each of the X , Y and Z directions. The three atoms surrounding the core on the first and third layers were again fixed in Z coordinate. The zero-point energy is given by

$$E_z = \frac{1}{2} \sum_{i=1}^3 \frac{h}{2\pi} \sqrt{k_i/m_C},$$

where k_i are the eigenvalues of the Hessian and m_C is the mass of carbon.

8 Bibliography

References

- [1] Steve Ooi, Junbiao Lai, Sebastián Restrepo, Rose Yan, and Erik Vegter. Dark etching regions under rolling contact fatigue: a review. page 20, 2019.

- [2] H. Fu, E.I. Galindo-Nava, and P.E.J. Rivera-Díaz del Castillo. Modelling and characterisation of stress-induced carbide precipitation in bearing steels under rolling contact fatigue. *Acta Materialia*, 128:176–187, April 2017.
- [3] A. H. King and J. L. O’Brian. *Microstructural Alterations in Rolling Contact Fatigue*, pages 74–74–15. Advances in Electron Metallography: Vol. 6. ASTM International, nil.
- [4] A. B. Jones. *Metallographic Observations of Ball Bearing Fatigue Phenomena*, pages 35–35–18. Symposium on Testing of Bearings. ASTM International, nil.
- [5] J. J. Bush, W. L. Grube, and G. H. Robinson. Microstructural, micro-hardness and residual stress changes due to rolling contact. *Tribology*, 3(4):249, 1970.
- [6] H. Swahn, P. C. Becker, and O. Vingsbo. Martensite decay during rolling contact fatigue in ball bearings. *Metallurgical Transactions A*, 7(8):1099–1110, August 1976.
- [7] AP Voskamp. Fatigue and material response in rolling contact. 1997.
- [8] A. P. Voskamp and E. J. Mittemeijer. State of residual stress induced by cyclic rolling contact loading. *Materials Science and Technology*, 13(5):430–438, 1997.
- [9] I Polonsky. On white etching band formation in rolling bearings. *Journal of the Mechanics and Physics of Solids*, 43(4):637–669, 1995.
- [10] Viktorija Smelova, Alexander Schwedt, Ling Wang, Walter Holweger, and Joachim Mayer. Electron microscopy investigations of microstructural alterations due to classical rolling contact fatigue (rcf) in martensitic aisi 52100 bearing steel. *International Journal of Fatigue*, 98(nil):142–154, 2017.
- [11] Ragnar Österlund and Olof Vingsbo. Phase changes in fatigued ball bearings. *Metallurgical Transactions A*, 11(5):701–707, May 1980.
- [12] N. Mitamura, H. Hidaka, and Setsuo Takaki. Microstructural development in bearing steel during rolling contact fatigue. *Materials Science Forum*, 539-543:4255–4260, Mar 2007.
- [13] Hanwei Fu, Wenwen Song, Enrique I. Galindo-Nava, and Pedro E.J. Rivera-Díaz del Castillo. Strain-induced martensite decay in bearing steels under rolling contact fatigue: Modelling and atomic-scale characterisation. *Acta Materialia*, 139(nil):163–173, 2017.

- [14] Anurag Warhadpande, Farshid Sadeghi, and Ryan D. Evans. Microstructural alterations in bearing steels under rolling contact fatigue part 1—historical overview. *Tribology Transactions*, 56(3):349–358, May 2013.
- [15] Anurag Warhadpande, Farshid Sadeghi, and Ryan D. Evans. Microstructural alterations in bearing steels under rolling contact fatigue: Part 2—diffusion-based modeling approach. *Tribology Transactions*, 57(1):66–76, November 2013.
- [16] A. P. Voskamp, R. Österlund, P. C. Becker, and O. Vingsbo. Gradual changes in residual stress and microstructure during contact fatigue in ball bearings. *Metals Technology*, 7(1):14–21, 1980.
- [17] S.H. Hashemi. Strength-hardness statistical correlation in api x65 steel. *Materials Science and Engineering: A*, 528(3):1648–1655, 2011.
- [18] H. K. D. H. Bhadeshia. Solution to the bagaryatskii and isaichev ferrite–cementite orientation relationship problem. *Materials Science and Technology*, 34(14):1666–1668, May 2018.
- [19] A. T. Paxton and C. Elsässer. Analysis of a carbon dimer bound to a vacancy in iron using density functional theory and a tight binding model. *Physical Review B*, 87(22), June 2013.
- [20] Lisa Ventelon, B. Lüthi, E. Clouet, L. Proville, B. Legrand, D. Rodney, and F. Willaime. Dislocation core reconstruction induced by carbon segregation in bcc iron. *Physical Review B*, 91(22), June 2015.
- [21] M. Itakura, H. Kaburaki, M. Yamaguchi, and T. Okita. The effect of hydrogen atoms on the screw dislocation mobility in bcc iron: a first-principles study. *Acta Materialia*, 61(18):6857–6867, 2013.
- [22] M. Itakura, H. Kaburaki, and M. Yamaguchi. First-principles study on the mobility of screw dislocations in bcc iron. *Acta Materialia*, 60(9):3698–3710, May 2012.
- [23] Emmanuel Clouet. Screw dislocation in zirconium: An ab initio study. *Physical Review B - Condensed Matter and Materials Physics*, 86(14):1–11, 2012.
- [24] Vasily Bulatov. *Computer Simulations of Dislocations (Oxford Series on Materials Modelling)*. Oxford University Press, dec 2006.
- [25] P.M. Anderson, J.P. Hirth, and J. Lothe. *Theory of Dislocations*. Cambridge University Press, 2017.

- [26] S. Morito, J. Nishikawa, and T. Maki. Dislocation density within lath martensite in fe-c and fe-ni alloys. *ISIJ International*, 43(9):1475–1477, 2003.
- [27] E. Simpson. *A Tight Binding Study of Dislocations in Iron and Their Interactions with Hydrogen*. PhD thesis, King’s College London, 2019.
- [28] M. I. Mendelev, S. Han, D. J. Srolovitz, G. J. Ackland, D. Y. Sun, and M. Asta. Development of new interatomic potentials appropriate for crystalline and liquid iron. *Philosophical Magazine*, 83(35):3977–3994, December 2003.
- [29] A. T. Paxton and C. Elsässer. Electronic structure and total energy of interstitial hydrogen in iron: Tight-binding models. *Physical Review B*, 82(23), December 2010.
- [30] David Rodney and Laurent Proville. Stress-dependent peierls potential: Influence on kink-pair activation. *Physical Review B*, 79(9), March 2009.
- [31] Emmanuel Clouet, Sébastien Garruchet, Hoang Nguyen, Michel Perez, and Charlotte S. Becquart. Dislocation interaction with c in -fe: A comparison between atomic simulations and elasticity theory. *Acta Materialia*, 56(14):3450–3460, August 2008.
- [32] C.S. Becquart, J.M. Raulot, G. Bencteux, C. Domain, M. Perez, S. Garruchet, and H. Nguyen. Atomistic modeling of an fe system with a small concentration of c. *Computational Materials Science*, 40(1):119–129, July 2007.
- [33] Y. Hanlummyuang, P.A. Gordon, T. Neeraj, and D.C. Chrzan. Interactions between carbon solutes and dislocations in bcc iron. *Acta Materialia*, 58(16):5481–5490, September 2010.
- [34] Stela Makri, Christoph Ortner, and James R. Kermode. A preconditioning scheme for minimum energy path finding methods. *The Journal of Chemical Physics*, 150(9):094109, March 2019.
- [35] W.A Spitzig and A.S Keh. Orientation dependence of the strain-rate sensitivity and thermally activated flow in iron single crystals. *Acta Metallurgica*, 18(9):1021–1033, Sep 1970.
- [36] Lisa Ventelon, F. Willaime, E. Clouet, and D. Rodney. Ab initio investigation of the peierls potential of screw dislocations in bcc fe and w. *Acta Materialia*, 61(11):3973–3985, Jun 2013.
- [37] Gh. Ali Nematollahi, Blazej Grabowski, Dierk Raabe, and Jörg Neugebauer. Multiscale description of carbon-supersaturated ferrite in severely drawn pearlitic wires. *Acta Materialia*, 111:321–334, June 2016.

- [38] B Lüthi, F Berthier, L Ventelon, B Legrand, D Rodney, and F Willaime. Ab initio thermodynamics of carbon segregation on dislocation cores in bcc iron. *Modelling and Simulation in Materials Science and Engineering*, 27(7):074002, July 2019.
- [39] P. Maugis and D. Kandaskalov. Revisiting the pressure effect on carbon migration in iron. *Materials Letters*, 270:127725, July 2020.
- [40] Wei Cai, Vasily V. Bulatov, Jinpeng Chang, Ju Li, and Sidney Yip. Periodic image effects in dislocation modelling. *Philosophical Magazine*, 83(5):539–567, January 2003.